Vibrational spectroscopy of $CaZrO_3$ single crystals

1998 J. Phys.: Condens. Matter 10 7501

(http://iopscience.iop.org/0953-8984/10/33/019)

J. Phys.: Condens. Matter **10** (1998) 7501–7510. Printed in the UK PII: S0953-8984(98)93846-2

Vibrational spectroscopy of $CaZrO_3$ single crystals

V M Orera†, C Pecharromán‡, J I Peña†, R I Merino† and C J Serna‡

† Instituto de Ciencia de Materiales de Aragón, CSIC-Universidad de Zaragoza, 50009 Zaragoza, Spain

‡ Instituto de Ciencia de Materiales (CSIC), Campus Universitario de Cantoblanco, 28049 Madrid, Spain

Received 29 April 1998

Abstract. $CaZrO_3$ single crystals were grown by the laser floating zone method. Polarized Raman spectra were measured and interpreted consistently with the *Pcmn* crystal space group. Up to 16 Raman modes were identified and their symmetry assigned. The infrared optical constants of $CaZrO_3$ were determined from the analysis of the reflectance spectra of single crystals and powders. In the latter case, an effective medium theory was used to analyse the reflectance spectrum. Assignment of the infrared mode symmetry was performed with the help of a theoretical calculation of the vibrational modes.

1. Introduction

There is an increasing interest in calcium zirconate based systems for potential use in sensors and devices at high temperatures. In particular their high chemical stability and low partial electronic conductivity makes them suitable for oxygen probes working at elevated temperatures in low oxygen partial pressure atmospheres [1] and also doped with some trivalent ions such as In, Ga and Sc for monitoring hydrogen and water [2, 3].

Added interest comes from $CaZrO_3$ being a component phase of the ZrO_2–CaO eutectic. This material presents excellent mechanical, electrical and optical properties suitable for devices [4–6]. Also $CaZrO_3$ crystals are a good matrix for luminescent systems. In particular, we have recently studied the spectroscopic properties of Er doped $CaZrO_3$ crystals. The high emission efficiencies, good matrix transparency and narrow bands found in that system make it very promising for optical applications [7]. Er^{3+} vibronic side bands observed in Er doped $CaZrO_3$ and the unpolarized Raman spectrum of $CaZrO_3$ microphases in CaO–ZrO_2 eutectics are the only references about the vibrational spectrum of this compound [4, 7].

$CaZrO_3$ is a perovskite-type material (ABO_3) but, different from other members of the family, only a small number of investigations on this zirconate are found, presumably because its very high melting temperature (∼2600 K) has precluded up to now the preparation of crystals of suitable size. Consequently, most structural and transport studies were performed using either powdered or eutectic samples.

$CaZrO_3$ crystal symmetry has been definitively established by convergent-beam electron diffraction in the directionally solidified ZrO_2–CaO eutectic as the *Pcmn* space group [8]. Unit cell parameters determined by powder neutron diffraction are $a = 0.55912(1)$, $b = 0.80171(2)$ and $c = 0.57616(1)$ nm [9].

0953-8984/98/337501+10$19.50

Success in growing $CaZrO_3$ single crystals of suitable size and with a small amount of defects to perform optical polarization studies, by the laser floating zone method (LFZ) [7], allows us to undertake in the present work the problem of determining the vibrational modes, including symmetry assignment, of this compound. For this purpose we apply Raman and infrared (I.R.) spectroscopy.

2. Experimental details

$CaZrO_3$ single crystal fibres were grown using an LFZ technique described elsewhere [10]. Sintered ceramic precursors of cylindrical shape were melted by CO_2 laser radiation. Radiation was focused onto a reduced zone ($\approx$1 mm long) supported by surface tension between feed ceramic and growing crystal. Large thermal gradients permit relatively high growth rates from 30 to 100 mm h^{-1}. The process was performed in an $N_2 + O_2$ synthetic air mixture. Very good optical quality crystals with cylindrical shape 50 mm long and 2 mm in diameter were obtained.

X-ray powder diffraction (XRD) patterns were recorded on ground samples in a Rigaku CD 2455D 6 x-ray diffractometer using Cu Kα radiation. The pattern did not present any other than the orthorhombic *Pcmn* $CaZrO_3$ phase. Sample orientation was checked using the back-reflection Laue method.

Polarized Raman spectra were measured at 300 K in a backscattering geometry, in a Dilor XY spectrometer with diode array multichannel detector and a $\times 50$ microscope objective lens. The light power at the sample was of the order of 50 mW and the spectral resolution better than 3 cm^{-1}.

To measure the reflectance spectrum, one longitudinal crystal section of about 5×1 mm^2 was cut and polished to obtain a perfect specular reflectance in the infrared region. Compressed pellets of $CaZrO_3$ powder, with a good quality specular surface, were also used for these experiments.

The reflectivity infrared spectra of the samples were recorded in the 120 to 1200 cm^{-1} range in Nicolet 20 SXC and 20 F Fourier Transform spectrometers, equipped with an Specac specular reflectance cell, which has a fixed incident angle of 12°. Infrared polarizers of metallic wire in a KBr matrix were used.

3. Theoretical background

At 300 K the structure of $CaZrO_3$ belongs to the D_{2h}^{16} (*Pcmn*) symmetry group. The crystal structure is depicted in figure 1. The orthorhombic unit cell contains four formulae with four different ion positions. Zr^{4+} is sited in the symmetry centre 4b position, Ca^{2+} and the four 'apical' oxygen ions O(1) in the symmetry plane 4c site and the remaining eight oxygen ions O(2) in the position 8d. The low symmetry phases of ABX_3 perovskites are usually understood in terms of condensation of BX_6 octahedron rotations around the cubic axes. The orthorhombic *Pcmn* structure results from two equivalent anti-phase tilts around the x' and z' cubic axes and an in-phase tilt around the b axis ($a^-b^+a^-$ in Glazer notation [11]). So, in the orthorhombic phase the pseudocubic y' axis is parallel to the orthorhombic $y = [010]$ axis with x' and z' nearly parallel to [101] and $[10\bar{1}]$ orthorhombic axes.

Standard group theory analysis yields the following zone centre lattice modes and optical activities for this space group:

$$\Gamma = 7A_g + 5B_{1g} + 7B_{2g} + 5B_{3g} + 8A_u + 10B_{1u} + 8B_{2u} + 10B_{3u} \qquad (1)$$

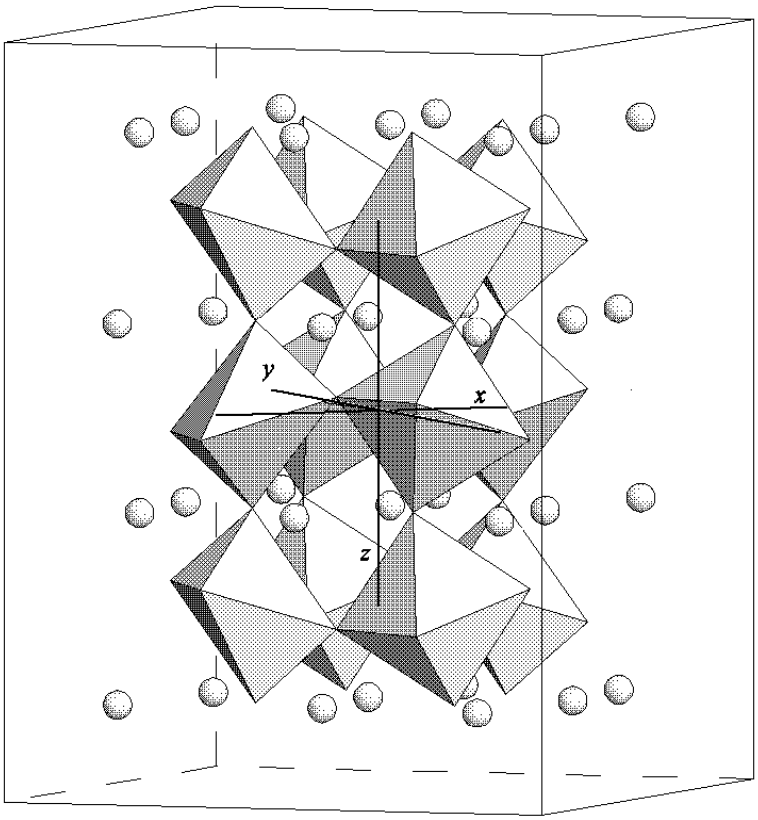

Figure 1. Structure of orthorhombic $CaZrO_3$. Octahedrons correspond to Zr^{4+} while Ca^{2+} appear as spheres. In the image orthorhombic axes are displayed and the y-axis is in the vertical orientation. In addition, cubic orientations are given by the external frame.

hence 24 Raman active modes (R), 25 infrared active modes (IR), eight non-active A_u and three ($B_{1u} + B_{2u} + B_{3u}$) translational modes.

The corresponding orthorhombic Raman tensors **T** referred to the (x, y, z) orthorhombic axes are:

$$\underset{A_{1g}}{\begin{bmatrix} a & & \\ & b & \\ & & c \end{bmatrix}} \quad \underset{B_{1g}}{\begin{bmatrix} & d & \\ d & & \\ & & \end{bmatrix}} \quad \underset{B_{2g}}{\begin{bmatrix} & & e \\ & & \\ e & & \end{bmatrix}} \quad \underset{B_{3g}}{\begin{bmatrix} & & \\ & & f \\ & f & \end{bmatrix}}$$

and referred to the (x', y, z') pseudocubic reference system:

$$\underset{A_{1g}}{\frac{1}{2}\begin{bmatrix} a+c & & -a+c \\ & 2b & \\ -a+c & & a+c \end{bmatrix}} \quad \underset{B_{1g}}{\frac{1}{\sqrt{2}}\begin{bmatrix} & d & \\ d & & -d \\ & -d & \end{bmatrix}} \quad \underset{B_{2g}}{\begin{bmatrix} e & & \\ & & \\ & & -e \end{bmatrix}} \quad \underset{B_{3g}}{\frac{1}{\sqrt{2}}\begin{bmatrix} & f & \\ f & & f \\ & f & \end{bmatrix}}.$$

The intensity of the Raman peaks is:

$$I \propto |\boldsymbol{e}_s \tilde{T} \boldsymbol{e}_i|^2 \tag{2}$$

$\boldsymbol{e}_s$ and $\boldsymbol{e}_i$ being the scattered and incident light polarization respectively.

The IR modes are polarized parallel to the orthorhombic x, y and z axes (modes B_{1u}, B_{2u} and B_{3u} respectively).

The IR optical constants of $CaZrO_3$ were determined from IR near normal reflectance experiments. We performed a least square refinement of the reflectance data using the Fresnel relation between the reflectance at normal incidence and the dielectric constant:

$$R = \left| \frac{\sqrt{\langle\varepsilon\rangle} - 1}{\sqrt{\langle\varepsilon\rangle} + 1} \right|^2. \tag{3}$$

The classic expression for the dielectric constant of a solid is assumed to be a superposition of N harmonic oscillators

$$\varepsilon(\omega) = \varepsilon_\infty + \sum_{k=1}^{N} \frac{\Delta\varepsilon_k \omega_{Tk}^2}{\omega_{Tk}^2 - \omega^2 - \mathrm{i}\gamma_k\omega} \tag{4}$$

where $\Delta\varepsilon_k$, ω_{Tk} and γ_k respectively are the oscillator strength, the transverse frequency and the damping constant of the kth mode.

This expression fails when it is applied to modes in which the spectral distance $\omega_{Lk} - \omega_{Tk}$ is large. In such cases, the damping function of each mode could not be taken as constant, but they depend on the frequency. Several authors found that in these cases it is possible to introduce an additional damping constant for the longitudinal kth mode [12, 13] by factorization of (4):

$$\varepsilon = \varepsilon_\infty \prod_{k=1}^{N} \frac{\omega_{Lk}^2 - \omega^2 - \mathrm{i}\gamma_{Lk}\omega}{\omega_{Tk}^2 - \omega^2 - \mathrm{i}\gamma_{Tk}\omega} = \varepsilon_\infty \prod_{k=1}^{N} \left[1 + \frac{\omega_{Lk}^2 - \omega_{Tk}^2 - \mathrm{i}(\gamma_{Lk} - \gamma_{Tk})\omega}{\omega_{Tk}^2 - \omega^2 - \mathrm{i}\gamma_{Tk}\omega} \right] \tag{5}$$

where ω_{Lk} and γ_{Lk} respectively are the longitudinal frequency and the damping factor of the kth mode. This formula, which satisfies the generalized Lydanne–Sachs–Teller relationships, reduces to (4) when $N = 1$ and $\gamma_L = \gamma_T$. In the expression (5), the longitudinal frequencies, ω_{Lk}, correspond to the zeros of the dielectric function. This formulation has been able to successfully fit the single crystal reflectance spectra of several substances with perovskite structure such as $SrTiO_3$ [14]. However, this model has the serious drawback that it may produce spectral regions with a negative imaginary part of the dielectric constant. In order to avoid this situation, these two relationships must be simultaneously satisfied for all modes [13]:

$$\gamma_{Lk} \geqslant \gamma_{Tk} \qquad \text{and} \qquad \frac{\gamma_{Tk}}{\gamma_{Lk}} \geqslant \left(\frac{\omega_{Tk}}{\omega_{Lk}} \right)^2. \tag{6}$$

However, in the case where the number of modes is larger than one, even if the former conditions are satisfied, negative values of the imaginary part of the dielectric function could arise when a strong kth mode is close to a heavily damped k'th mode. In this situation, the imaginary part of the total permittivity can be negative around the minimum of the real part of the dielectric constant of the kth mode. This condition can be easily checked by direct evaluation of the product:

$$\mathrm{Im}\,[\varepsilon_k(\omega)\varepsilon_{k'}(\omega)] = \varepsilon_k'(\omega)\varepsilon_{k'}''(\omega) + \varepsilon_k''(\omega)\varepsilon_{k'}'(\omega). \tag{7}$$

when $\varepsilon_k'(\omega)$ is negative and $\varepsilon_{k'}''(\omega)$ is large enough, their product could make (7) negative. That condition cannot be avoided by using a factorized expression such as (5) and the only way to overcome this problem is to evaluate the dielectric constant as a sum of oscillators instead of a product. This is why we proposed to use a hybrid expression, which evaluates

the dielectric function as a sum of different modes, but it distinguishes between transverse and longitudinal damping. (5) can be written as:

$$\varepsilon = \varepsilon_\infty \left[1 + \sum_{k=1}^{N} \frac{\omega_{Lk}^2 - \omega_{Tk}^2 - \mathrm{i}(\gamma_{Lk} - \gamma_{Tk})\omega}{\omega_{Tk}^2 - \omega^2 - \mathrm{i}\gamma_{Tk}\omega} + \cdots \right]. \tag{8}$$

Within this approximation we have dropped the terms where cross oscillator products appear. If $N = 1$ (8) and (5) coincide, and when $\gamma_{Tk} = \gamma_{Lk}$ the classical expression (4) is recovered. It should be pointed out that in this expression ω_{Lk} is no longer a zero of the multimodal function $\varepsilon(\omega)$ but only that of the dielectric function of the kth mode. It should be remembered that (8) should also satisfy equations (6) to avoid unphysical features. Because these conditions are somewhat arbitrary, i.e. there is no physical statement that forces to the longitudinal damping to be larger than the transversal one, we have instead decided to drop all the restrictions and wisely modify the values of damping functions outside the spectral region from ω_{Tk} to ω_{Lk}. In general, the dielectric function must satisfy this condition to avoid negative values of the imaginary part of the permittivity.

$$(\gamma_{Tk}\omega_{Lk}^2 - \gamma_{Lk}\omega_{Tk}^2) + \omega^2(\gamma_{Lk} - \gamma_{Tk}) < 0. \tag{9}$$

This equation defines a frequency for each mode, at which the imaginary part of the dielectric constant changes its sign.

$$\omega_{Ck}^2 = \left(\frac{\gamma_{Tk}\omega_{Lk}^2 - \gamma_{Lk}\omega_{Tk}^2}{\gamma_{Tk} - \gamma_{Lk}} \right). \tag{10}$$

It can be easily shown that this frequency never lies in the spectral interval defined by $[\omega_{Tk}, \omega_{Lk}]$. In the case when frequency is smaller than ω_{Tk}, the longitudinal damping function, $\gamma_{Lk}(\omega)$, which in (5) is a constant function, now has been continuously modified, from ω_{Tk} to ω_{Ck}, so that (9) is never smaller than zero and the damping function is continuous in the whole range of frequencies. In contrast, if $\omega_{Ck} > \omega_{Lk}$ we have modified $\gamma_{Tk}(\omega)$ from ω_{Lk} to ω_{Ck}. In both cases, damping functions satisfy:

$$\gamma_{Tk}(\omega_{Ck}) = \gamma_{Lk}(\omega_{Ck}) \tag{11}$$

In our case, the small size of the sample and its orientation prevent us from obtaining reliable quantitative reflectance data on a single crystal. Hence, to calculate the IR mode frequency we have also measured the reflectance of a pellet of compressed $CaZrO_3$ powder. The spectrum was analysed by an effective medium theory, which has been previously successfully used to determine the dielectric properties of small powder samples [15]. Details of this procedure are given elsewhere [16–18].

Assignment of the Brillouin zone centre $CaZrO_3$ phonon modes was performed by using the VIBRAT program [19]. This method calculates the frequency and symmetry of the modes taking into account the crystal structure and the atomic interactions between nearest neighbours. First neighbour potentials are obtained by fitting the calculated frequencies and symmetries to those of some well assigned vibrational modes obtained from experiments.

4. Results and discussion

Crystals grow with one of the pseudocubic axis nearly parallel to the growth direction (cylinder axis). Samples present large grains ($\sim$1 mm^3) keeping common the growth direction but with the y orthorhombic axis lying in the plane perpendicular to the pseudocubic growth axis and orthogonal between adjacent grains. The microstructure can be visualized by placing the sample between crossed polarizers and is a result of the normal

cubic perovskite high temperature phase to low temperature orthorhombic phase transition at 2023 K [20]. Stresses related to the directional solidification procedure produce the predominance of twins with a common pseudocubic axis. Two different types of twin among the six predicted by space group considerations are observed [8]. Using the sample capability to cleave along the pseudocubic planes we obtained small cubes where pseudocubic axes were easily identified. The orthorhombic y axis coincides with the cubic y' axis whereas the x and z orthorhombic ones are lying in the $x'z'$ plane near to 45° from the pseudocubic axes.

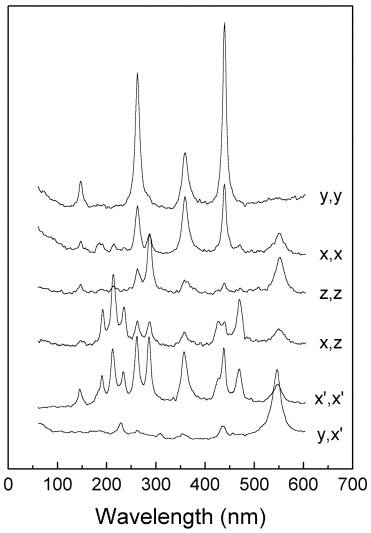

Figure 2. Raman spectra of $CaZrO_3$ single crystals measured at 300 K for different polarization configurations.

Raman lattice modes appear at energies below 600 cm^{-1} in agreement with previously observed Er^{3+} vibronic structure in this crystal [7]. In figure 2 we show the Raman spectra down to 50 cm^{-1} of $CaZrO_3$ taken at 300 K with different polarizations either parallel to the orthorhombic cell axes labelled xx, yy, zz and xz or parallel to the cube axes $x'x'$ and yx' (we shall denote by $\alpha\beta$ the experimental configuration, where α and β stand for the incoming and outgoing electric field polarization, respectively). Using equation (1) we can predict the Raman activity of a given mode for each experimental geometry we use as follows:

Polarization	A_g	B_{1g}	B_{2g}	B_{3g}
xx	a^2	—	—	—
yy	b^2	—	—	—
zz	c^2	—	—	—
xz	—	—	e^2	—
$x'x'$	$(a+c)^2/4$	—	e^2	—
yx'	—	$d^2/2$	—	$f^2/2$

The spectra do not depend on the excitation wavelength. They consist of up to 14 well resolved peaks; their frequency and polarization are listed in table 1. Most of the peaks are completely polarized. Since the Raman spectra for different polarizations are different we are certain that we measured a single-domain crystal where orthorhombic axes are well differentiated. Though the orthorhombic directions could be identified by x-ray diffraction,

Table 1. Mode frequency, polarization and symmetry assignments of $CaZrO_3$ single crystal Raman peaks.

Frequency (cm^{-1})	Polarization	Symmetry
145	yy, $x'x'$	A_g
190	xz, $x'x'$	B_{2g}
212	xz, $x'x'$	B_{2g}
227	yx'	B_{1g} or B_{3g}
234	xz, $x'x'$	B_{2g}
262.5	yy, zz, xz, $x'x'$	A_g
286.5	xx, zz, xz, $x'x'$	A_g
305	yx'	B_{1g} or B_{3g}
358	yy, zz, $x'x'$	A_g
418	xz, $x'x'$	B_{2g}
439	yy, zz, $x'x'$, yx'	$A_g + B_{1g}$ or B_{3g}
469	xz, $x'x'$	B_{2g}
543	xx, zz, xz, $x'x'$	$A_g + B_{2g}$
547	yx'	B_{1g} or B_{3g}

it was not possible to distinguish between x and z axes. Then, although the xx and zz spectra were found to be different we could not distinguish between B_{1g} and B_{3g} modes.

The assignment of the lattice mode symmetry for D_{2h}^{16} space group taking into account the Raman activities given above can be also found in table 1. Some intensity of the A_g modes is observed for cross xz polarization which may introduce some uncertainty in the assignment of the B_{2g} component of the 543 cm^{-1} band. This is due to depolarizing effects in the experimental set-up allowing for a part of the strong A_g component going into the crossed configuration. Instead, the 439 cm^{-1} band has a clear $A_g + B_{1g}$ or B_{3g} character. In total we identified 16 of 24 possible Raman modes.

Due to crystal growth procedure and twin structure, the single crystal sample used for IR measurements only permits $E \parallel x'$ ($B_{1u} + B_{3u}$ modes) and $E \perp x'$ (all three IR active modes) measurements. The $CaZrO_3$ single crystal reflectances for the two measured polarizations are plotted in figure 3(b). For the reason given above, a quantitative analysis of these measurements was not attempted. Instead, we include some approximate frequency values estimated directly from the spectra.

The reflectance spectrum from a pellet of $CaZrO_3$ powder is given in figure 3(a). In this case we were able to measure down to 120 cm^{-1}. Using the same procedure as outlined above for spherical shaped particles we fitted the spectrum with 12 optical modes whose frequencies and damping factors are given in table 2 (see (8)). The comparison between experimental and calculated reflectance given in figure 3(a) is fairly good. The imaginary part of the dielectric constant, calculated from fitting parameters, is given in figure 4(a). In such a picture we can distinguish three families of modes (from 100 to 250, from 300 to 400 and from 450 to 600 cm^{-1}), which correspond to the three IR modes of the perovskite structure.

In order to check the results of the fitting, we have calculated the average reflectance spectrum (filling factor $f = 1$) from fitted parameters, and we have compared it with the single crystal polarized measurements (figure 3(b)). As expected, the single crystal $E \perp x'$ spectrum is very similar to the simulated averaged spectrum. However, peaks at 388, 366, 270, 249 and 309 cm^{-1} are resolved in $E \parallel x'$. These modes must be B_{1u} or B_{3u} symmetry.

To further confirm the results of the fitting, we have dispersed the powdered sample in KBr and polyethylene. We made two pellets by cold pressing, and IR absorbance spectra of the samples were recorded (figure 4(b)). A theoretical absorbance spectrum was calculated

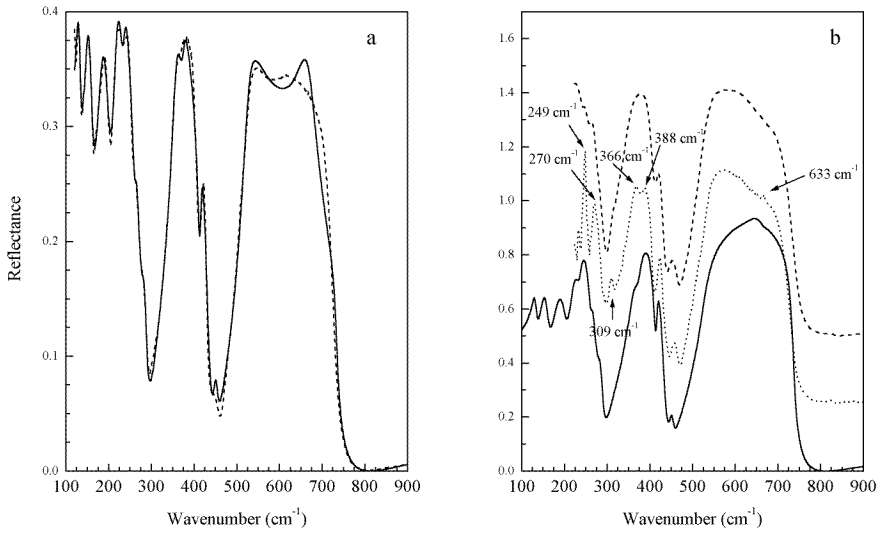

Figure 3. (a) (left) Infrared reflectance spectrum of the $CaZrO_3$ powder measured at 300 K: experimental (dashed line) and calculated (continuous line) for spheres, through an effective medium theory with the optical parameters listed in table 2; (b) (right) infrared reflectance spectrum of the $CaZrO_3$ single crystals measured at 300 K for $E \perp x'$ (dashed line) and $E \parallel x'$ (dotted line) polarization configurations in comparison with single crystal calculation from parameters obtained from powder reflectance spectrum fitting.

Table 2. Parameters of the oscillators related to IR phonon modes used to fit the $CaZrO_3$ powder reflectance spectrum of figure 3(a). f represents the filling factor, f_c the percolation threshold used in the EMT and R the goodness of fit. All frequencies and damping constants are given in cm^{-1}.

$f = 0.56$	$f_c = 0.44$	$\varepsilon_\infty = 3.91 \pm 0.03$		$R = 4.7\%$
ω_T	γ_T	$\omega_L - \omega_T$	γ_L	Assignation
130.4 ± 0.6	11.3 ± 1.2	50.4 ± 5	8 ± 26	B_{3u}
152.2 ± 0.7	17.5 ± 1.7	76 ± 8	16 ± 22	B_{1u}, B_{2u}, B_{3u}
186.4 ± 1.0	27 ± 2	99 ± 9	21 ± 20	B_{1u}, B_{2u}, B_{3u}
219.1 ± 1.0	20.9 ± 1.8	79 ± 10	15 ± 21	B_{1u}
237.3 ± 1.5	15 ± 3	20 ± 7	2 ± 14	B_{1u}
263 ± 3	11 ± 4	3.2 ± 1.6	11 ± 6	B_{3u}
282.2 ± 1.7	17 ± 6	4.7 ± 2.0	11 ± 3	B_{3u}
357.6 ± 0.6	24.3 ± 1.2	96 ± 4	10 ± 5	B_{1u}
375.7 ± 1.0	18 ± 3	19 ± 4	5 ± 4	B_{3u}
416.0 ± 0.9	8.2 ± 0.9	3.0 ± 0.3	7.3 ± 1.1	B_{1u}, B_{2u}, B_{3u}
451 ± 2	12 ± 3	2.0 ± 0.4	11 ± 3	B_{1u}, B_{3u}
525.0 ± 0.4	34.4 ± 1.0	108.2 ± 1.2	9.5 ± 1.2	B_{1u}, B_{2u}, B_{3u}

by using the effective medium theory, but in this case, a distribution with filling factor of 0.55 and 0.3 was used. These unusually high values of concentration, which are usually found in massive powder pellets, can be explained as an effect of local aggregation. This effect is commonly found in absorbance spectra of pressed pellets [21] when most of the powder particles are not dispersed in the transparent matrix, but they remain aggregated in clusters. In general, the agreement between both spectra is satisfactory. However, in the long tail of the 525 cm^{-1} mode a shoulder around 633 cm^{-1} seems to appear. This shoulder also appears in single crystal spectra, and even in the powder reflectance spectrum. This

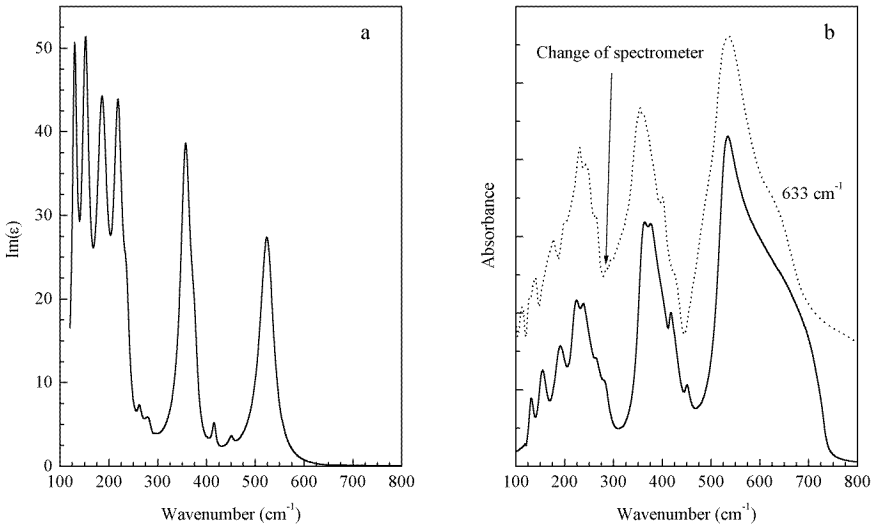

Figure 4. (a) (left) Imaginary part of dielectric constant calculated from parameters listed in table 2; (b) (right) experimental absorption spectrum of $CaZrO_3$ powder dispersed in KBr and polyethylene (dashed line) and theoretical calculation (continuous line) from parameters listed in table 2.

Table 3. Raman and infrared frequencies (in cm^{-1}) observed and calculated by using the VIBRAT program for $CaZrO_3$. Symmetry mode assignment.

Raman			IR		
Calculated	Observed	Symmetry	Calculated	Observed	Symmetry
538.3	543.0[a]	A_g	544.6	525	B_{1u}
425.6	439.0[a]	A_g	450.6	451	B_{1u}
386.6	—	A_g	419.9	416	B_{1u}
344.2	358.0[a]	A_g	331.5	358 (366)	B_{1u}
278.1	286.5[a]	A_g	312.2	(309)	B_{1u}
228.4	262.5[a,b]	A_g	247.0	237 (249)	B_{1u}
143.4	145.0[a]	A_g	205.4	219	B_{1u}
479.7	—	B_{1g}	172.2	186	B_{1u}
410.0	—	B_{1g}	156.9	152	B_{1u}
380.2	—	B_{1g}	512.3	525	B_{2u}
304.8	305	B_{1g}	478.1	—	B_{2u}
241.0	227	B_{1g}	411.1	416	B_{2u}
537.6	543[a]	B_{2g}	323.9	—	B_{2u}
457.1	469[a]	B_{2g}	192.7	186	B_{2u}
412.6	418[a]	B_{2g}	158.0	152	B_{2u}
361.9	—	B_{2g}	98.5	—	B_{2u}
269.2	234[a,b]	B_{2g}	514.6	525	B_{3u}
224.9	212[a]	B_{2g}	447.5	451	B_{3u}
180.7	190[a]	B_{2g}	429.7	416	B_{3u}
495.3	547	B_{3g}	365.0	376 (388)	B_{3u}
452.7	439	B_{3g}	306.9	282 (270)	B_{3u}
386.5	—	B_{3g}	257.4	263	B_{3u}
327.0	—	B_{3g}	191.8	186	B_{3u}
154.6	—	B_{3g}	172.8	152	B_{3u}
			147.6	130	B_{3u}

[a] Mode used to obtain the vibration potential constants.
[b] Poor fitting. In brackets, modes resolved in the single crystal reflectance spectrum.

mode must have a very low oscillator strength, because it was not possible to introduce it into the fitting. The origin of this shoulder seems to be a combination mode, associated with

the main mode at 525 cm^{-1}. However, this additional mode is not enough to explain such a large broadening. In addition, the contribution of the large heterogeneous aggregation is also important in order to quantitatively explain the high frequency tail.

To complete the assignment of the symmetry of the modes we have performed a vibrational calculation at $k = 0$, as described in the previous section. The six A_g and six B_{2g} measured Raman modes were chosen to calculate the force constants. As the compound is highly ionic, only stretching Ca–O, Zr–O and O–O and bending O–Ca–O and O–Zr–O interactions were considered. The calculation results are presented in table 3 in comparison with the experimental results. In general the agreement can be considered very good.

Analysis of Raman modes describes these modes as Ca–O movements, while Zr^{4+} cations remain steady. It can be said that at frequencies higher than 350 cm^{-1} most of the modes are due to the oxygen sublattice, while at lower frequencies Raman activity is mainly due to Ca^{2+} movement.

IR active modes are somewhat similar to that of the cubic perovskite, in which only three active T_{1u} modes are present. These modes can be described, in decreasing frequency order, as: stretching of Ca–O (550 cm^{-1}), stretching of Zr–O (400 cm^{-1}) and stretching of Ca–Zr (150 cm^{-1}). The Zr–O frequency in $CaZrO_3$ is quite close to that of tetragonal ZrO_2 (460 cm^{-1}) [16]. Although in the orthorhombic structure there exist bending modes around 300 cm^{-1} and some other modes with mixed character, the general features of the orthorhombic structure follow approximately the same scheme which indicates that most IR modes are a simple splitting of cubic IR modes.

Acknowledgment

This work was supported by CICYT (Spain) grant MAT97-0673-CO2

References

[1] Janke D 1982 *Metall. Trans.* B **13** 227
[2] Yajima T, Kazcoka H, Yogo T and Iwahara H 1991 *Solid State Ion.* **47** 271
[3] Hibino T, Mizutani K, Yajima T and Iwahara H 1992 *Solid State Ion.* **57** 303
[4] Peña J I, Merino R I, de la Fuente G F and Orera V M 1996 *Adv. Mater.* **8** 909
[5] Merino R I, Peña J I, Orera V M and de la Fuente G F 1997 *Solid State Ion.* **100** 313
[6] Orera V M, Peña J I, Merino R I, Lázaro J A, Vallés J A and Rebolledo M A 1997 *Appl. Phys. Lett.* **71** 2746
[7] Merino R I, Pardo J A, Peña J I, de la Fuente G F, Larrea A and Orera V M 1997 *Phys. Rev.* B **56** 10 907
[8] Dravid V P, Sung C M, Notis M R and Lyman C E 1989 *Acta Crystallogr.* B **45** 218
[9] Koopmans H J A, van de Velde G M H and Gellings P J 1983 *Acta Crystallogr.* C **39** 1323
[10] de la Fuente G F, Diez J C, Angurel L A, Peña J I, Sotelo A and Navarro R 1995 *Adv. Mater.* **7** 853
[11] Glazer A M 1972 *Acta Crystallogr.* B **28** 3384
[12] Gervais F and Pirou B 1974 *Phys. Rev.* B **10** 1642
[13] Gervais F and Pirou B 1974 *J. Phys. C: Solid State Phys.* **7** 2374
[14] Servoin J L, Luspin Y and Gervais F 1981 *Phys. Rev.* B **22** 5501
[15] Pecharromán C, Ocaña M and Serna C J 1996 *J. Appl. Phys.* **80** 3479
[16] Pecharromán and Iglesias J E 1994 *Phys. Rev.* B **49** 7137
[17] Pecharromán C and Iglesias J E 1994 *J. Phys.: Condens. Matter* **6** 7125
[18] Pecharromán C, Gonzalez-Carreño T and Iglesias J E 1996 *J. Mater. Res.* **11** 127
[19] Dowty E 1987 *Phys. Chem. Miner.* **14** 67
[20] Stubican V 1986 *Science and Technology of Zirconia III* ed S Somiya, N Yamamoto and H Yanagida (Westerville, OH: American Ceramic Society) pp 71–82
[21] Pecharromán C and Iglesias J E 1996 *Appl. Spectrosc.* **50** 1553